

Soft Matter

Accepted Manuscript



This is an *Accepted Manuscript*, which has been through the Royal Society of Chemistry peer review process and has been accepted for publication.

Accepted Manuscripts are published online shortly after acceptance, before technical editing, formatting and proof reading. Using this free service, authors can make their results available to the community, in citable form, before we publish the edited article. We will replace this *Accepted Manuscript* with the edited and formatted *Advance Article* as soon as it is available.

You can find more information about *Accepted Manuscripts* in the [Information for Authors](#).

Please note that technical editing may introduce minor changes to the text and/or graphics, which may alter content. The journal's standard [Terms & Conditions](#) and the [Ethical guidelines](#) still apply. In no event shall the Royal Society of Chemistry be held responsible for any errors or omissions in this *Accepted Manuscript* or any consequences arising from the use of any information it contains.

Surface-Induced Phase Transitions of Wormlike Chains in Slit Confinement

Shiwei Ye,^(a) Pingwen Zhang,^{*(a)} and Jeff Z. Y. Chen^{*(b)}

Received Xth XXXXXXXXXXXX 20XX, Accepted Xth XXXXXXXXXXXX 20XX

First published on the web Xth XXXXXXXXXXXX 200X

DOI: 10.1039/b000000x

On the basis of a self-consistent field theory treatment of semi-flexible polymer chains, we analyze the effects of the flexibility on the structure of polymers sterically confined between two parallel, structureless walls separated by a distance. The model is built from a wormlike chain formalism which crosses over from the rod limit to the flexible limit, and the Onsager-type interaction which describes the orientation-dependent excluded-volume interaction. Three surface states were obtained from the numerical solution to the theory: uniaxial, biaxial, and condensed. As the overall density increases in such a lyotropic system, first order phase transitions between uniaxial-biaxial states, and biaxial-condensed states can occur.

1 Introduction

1.1 Nematic liquid crystals in a slit

The nematic state of a liquid crystal system consists of long molecules that are directionally aligned in one direction while the position of these molecules are randomly distributed. The introduction of a wall surface disrupts the otherwise uniform density distribution of the molecules in a bulk state [Fig. 1]. In his seminal work, using the Landau-de Gennes theory of thermotropic liquid crystals consisting of rigid molecules, Sheng demonstrated that near a *single* flat wall surface, several surface-induced structures displaying different orientational and wetting properties can be produced,^{1,2} depending on the wall-anchoring properties. The surface-induced structures can mutually phase transit into each other, yielding a possible biaxial state near the surface. Indeed, other studies of models of a similar nature have arrived at the same conclusion.^{3–6} Using a Mayer-Saupe type approach, Emelyanenko *et al.*⁷ have recently correlated the surface-transition theory with an experimental measurement on a thermotropic liquid crystal.⁸

In a lyotropic liquid crystal system, the molecular density is the control parameter, in comparison with a thermotropic system where the temperature is the control parameter.⁹ Using a molecular-level theoretical model that can be traced back to molecular-level parameters such as density and excluded-volume diameter, Chen and Cui demonstrated the phase transition between two surface phases in flexible lyotropic liquid-crystalline polymer solutions near a single hard wall surface.¹⁰ As matter of fact, these surface states in association

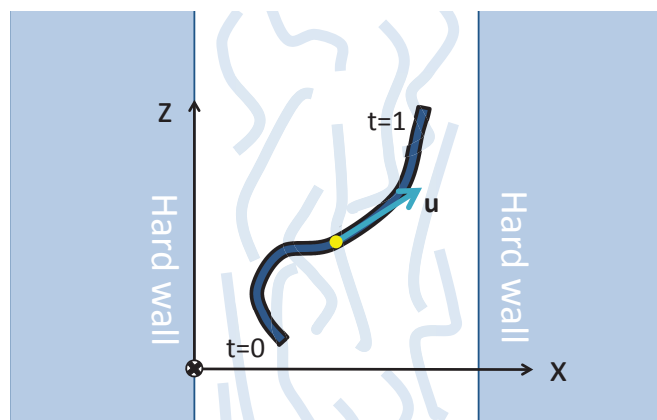


Fig. 1 Cross-section view of wormlike polymer chains confined in a slit between two parallel hard walls separated by a distance H . A coordinate system is set up such that the x -axis is along the surface normal. An arc-variable t is defined on the polymer chain starting from one terminal ($t = 0$) and ending at another ($t = 1$). The tangent direction of the chain \mathbf{u} is also shown.

with special orientational ordering are quite general in liquid crystals and can exist in lyotropic systems as well, which can exist in a liquid-crystal mixture¹¹ or a fluid of hard colloidal platelets. Directly using an Onsager functional for rigid rod-like molecules, a special case of the wormlike chain model in the rigid limit, Shundyak and van Roij reported that the surface a transition can happen when rigid rods are in contact with a soft wall.¹² Beyond such a mean-field type model, Monte Carlo simulations have been used as well to demonstrate the existence of wetting and capillary nematization of hard rods.¹³ The existence of the surface biaxial layer for liquid crystal rods was also shown in more complicated density-

^a LMAM and School of Mathematical Sciences, Peking University, Beijing, 100871, PRC. Email: pzhang@pku.edu.cn

^b Department of Physics and Astronomy, University of Waterloo, Ontario, Canada, N2L 3G1. Email: jeffchen@uwaterloo.ca

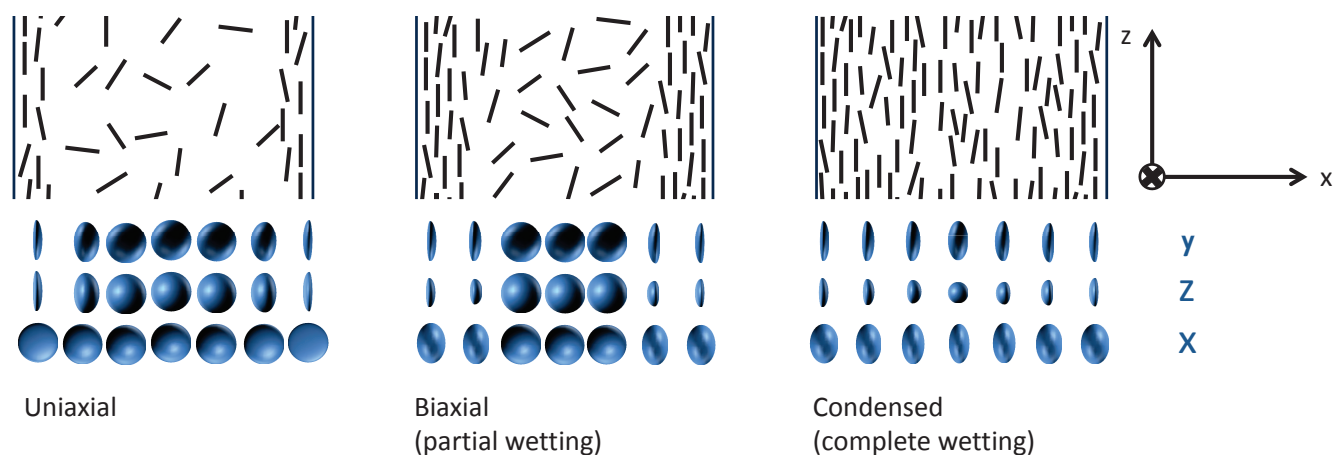


Fig. 2 Illustrations of the surface wetting states predicted from SCFT of wormlike polymers interacting with each other by the Onsager excluded volume interaction. On the top row, we illustrate the uniaxial state where the orientational distribution is symmetric about the x -axis, the biaxial state where the two surface layers display nematic ordering along the z -axis but the middle portion still stays at an isotropic state, and the condensed phase where the middle portion forms a nematic state with a nematic director in z , similar to a bulk nematic phase. On the second, third, fourth rows, the distribution function is projected in three different perspectives, viewed from the y -axis, z -axis, and x -axis. Lines are used in the sketches to demonstrate the orientational distribution; they do not represent images of the molecules — except for the $\alpha \ll 1$ limit.

functional theories.^{14–16}

The problem of wormlike polymers confined between *two* flat surfaces separated by a distance H provides another competing parameter, the slit width, which enriches the physical picture of surface transitions. van Roij *et al.* used Monte Carlo simulation and the Zwanzig model¹⁸ to demonstrate that lyotropic rigid rods in a slit display three different types of orientational phases (uniaxial, biaxial or condensed), separated by phase boundaries in a phase diagram.^{17,19} Using a self-consistent field theory coupled with the Onsager interaction for flexible wormlike liquid-crystal polymers, Chen *et al.* have found similar surface phases.^{20,21} Depending on the magnitude of the overall density, the system can display a typical orientational pattern which is schematically shown in Fig. 2. Recent Monte Carlo simulations on confined semiflexible chains have verified the existence of these surface states and the surface phase transitions between them.^{22–25} The uniaxial, biaxial, and condensed phases are called surface disordered, surface ordered, and nematic phases in the last three references. The phase diagram based on simulation results presented in Ref. 24 qualitatively matches the phase diagram based on mean-field theories presented in Refs. 20, 21. The basic structure is similar to those in Fig. 3. Table 1 summarizes these theoretical studies.

One major difference, though, is that the uniaxial-to-biaxial transition line was identified as a continuous transition in Refs. 17, 19, 23–25, whereas the same transition line was iden-

tified as a first-order transition in Refs. 21. To ensure that this is not caused by various degrees of flexibility

$$\alpha = L/2\lambda \quad (1)$$

where L is the molecule length and λ is the persistence length of a wormlike chain, here we examine the surface properties over the entire α range, with particular attention paid to the asymptotic rigid limit ($\alpha \ll 1$). The same self-consistent field theory (SCFT) is used, consistent with the model used in Refs. 20, 21 where only the $\alpha \gg 1$ limit was examined. Here, because a different numerical technique is used, we verify the phase diagram calculated in the $\alpha \gg 1$ limit. The theoretical framework can be found from Ref. 26 and is summarized in Appendix A. When the formalism is applied to the bulk state in the $\alpha \gg 1$ limit, the entire theory is reduced to the one used by Khokhlov and Semenov²⁷ for studying the isotropic-nematic phase transition of a flexible polymer solution, who incorporated the Onsager interaction which drives the phase transition.²⁸ Appendixes B and C review the bulk transition for any α determined in Ref. 29. For the slit confinement problem, we can use the slit width H as a scaling parameter, which makes the entire theory to depend on three parameters, α , L/H , and the density of the system; this can be found in Appendix D.

As will be discussed in more details below, using the numerical technique presented in Appendix E, we arrive at a similar conclusion, regardless the flexibility of the molecules

	$\alpha = L/2\lambda$	Zwanzig model	Onsager model	Monte Carlo
Rods	$\ll 1$	Ref. 17, 19	This work	Ref. 17, 19
Semiflexible polymers	any		This work	
Flexible polymers	$\gg 1$		Ref. 21	Ref. 24

Table 1 Theoretical studies of lyotropic wormlike polymers confined by a slit consisting of two hard walls, by using different models. The total length and persistence length of a polymer are L and λ .

in the system. Both uniaxial-biaxial and biaxial-condensed transition lines are of the first-order characteristics and they both terminate at critical points, as shown by filled symbols in Fig. 3. Figure 3(e) for $\alpha \gg 1$ is identical to the one in Ref. 21 where a completely different numerical method was used.

While all technical details are placed in Appendixes for interested readers, in Sect. 1.2 we first explain the orientational structures expected in each of these states. The main theoretical procedure is briefly reviewed in Sect. 1.3. The new numerical results for the limit $\alpha \ll 1$ are discussed and analyzed in Sect. 2. For semiflexible systems where $\alpha \neq 0$, we first review the $\alpha \gg 1$ case in Sect. 3.1, and then turn our attention to the crossover between the two asymptotic α limits, by noting a few outstanding features in the intermediate α systems, in Sect. 3.2.

1.2 Surface states and order parameters

Figure 1 is an illustration of the lyotropic system that is considered here. Wormlike molecules are placed inside the slit and they interact with each other by an excluded-volume interaction. The polymer segments experience steric repulsion from the confining walls which naturally forms a planar anchoring condition. No special anchoring preference is assumed at the wall and no other interactions (such as the van der Waals attraction) are considered. In a bulk phase, which is also relevant here for the $H/L \gg 1$ limit, below the isotropic-nematic transition point, the bulk of the liquid is at an isotropic state. In a low-density system, the orientational ordering of the molecules is symmetric about the wall normal and typically persists within a thin layer. In a system of rigid rods, the thickness of the layer can be a few times of L . In a system of semiflexible chains, the thickness of the ordered layer can be a few times of λ . The left panel of Fig. 2 illustrates this case. One principal order parameter is adequate for the description of this uniaxial (U) state.

As molecular density increases, the uniaxial state yields to the biaxial (B) state where a thicker layer of ordered polymer segments can now be seen. These layers accompany a density enhancement and contain nematic-like orientational ordering, aligned in a direction in parallel to the surface surface, the z axis. A typical structure is shown in the middle illustration of Fig. 2. The distribution function no longer has the rotational symmetry about the x axis. The central portion of the system

is still in its isotropic phase where the symmetry remains.

As the density further increases, the surface density enhancement layer grows in thickness. As the overall density approaches the vicinity of the bulk isotropic-nematic transition point, the entire system displays orientational ordering, and now the nematic state dominates the system. The surface layer grows rapidly, making a phase transition from a pre-wetting state to a complete wetting state. The right panel of Fig. 2 is an illustration for a confined liquid crystal at its condensed (C) state. The central portion of the the liquid no longer has a symmetry about the x axis in its orientational distribution function. Rather, the central portion now has a main orientational axis along the z axis and is uniaxial about z . The presence of the wall can now be viewed as an effect that makes the system biaxial, which has the same nature as the weak biaxiality that must be present at an isotropic-nematic interface in parallel to the main nematic director.^{30,31}

Hence the simplest measurement that can be used to distinguish the different surface states studied here is from examining the properties of the orientation order parameter, which is usually represented in a matrix form.³² The orientational states and definition of the axes illustrated in Fig. 2 give rise to a diagonalized order parameter matrix.

A polymer chain is made of monomeric segments. To understand the near-wall structure, we look into the orientational properties as a function of distance from the left wall, x . Across the slit, the left wall has the coordinate $x = 0$ and the right $x = H$. Let $\phi(x, \mathbf{u})$ be the segment distribution function at x for a segmental orientation specified by a tangent unit vector \mathbf{u} . These three diagonal orientational order parameters, S_x , S_y , and S_z can be defined by using the second-rank Legendre polynomial $P_2(\zeta) = \frac{1}{2}(3\zeta^2 - 1)$,

$$S_k(x) \equiv \frac{\int d\mathbf{u} P_2(\mathbf{u} \cdot \hat{\mathbf{k}}) \phi(x, \mathbf{u})}{\int d\mathbf{u} \phi(x, \mathbf{u})} \quad (2)$$

where $k = x, y, z$. Three unit vectors $\hat{\mathbf{k}} = \hat{x}, \hat{y}$, and \hat{z} along the x -, y -, and z -axes are used here.

Only two of these three functions are independent. The definition above yields the identity

$$S_x(x) + S_y(x) + S_z(x) = 0. \quad (3)$$

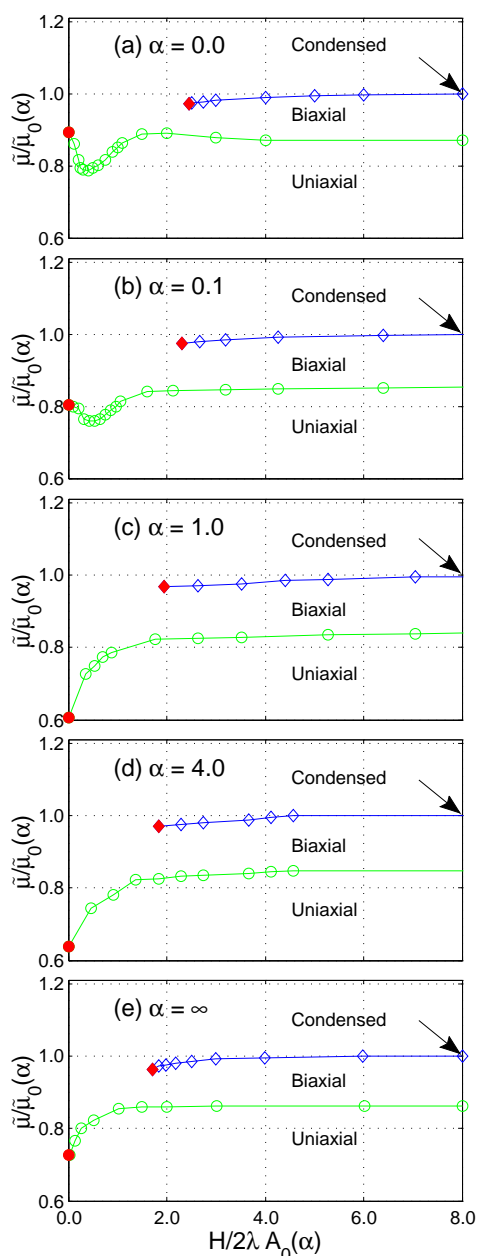


Fig. 3 Surface phase diagrams determined in this work, in terms of the reduced chemical potential $\tilde{\mu} = \beta\mu$ and reduced slit height H for systems composed of wormlike molecules of various degrees of flexibility: $\alpha = 0$ (rodlike), 0.1 (near-rodlike), 1.0 (semiflexible), 4.0 (near flexible), and ∞ (flexible). All phase diagrams contain three states illustrated in Fig. 2. Solid lines are interpolated, first-order phase boundaries crossing open symbols which are actually determined in numerical calculations. Filled symbols indicate terminal second-order transition points. Arrows indicate the first-order, bulk (i.e., $H = \infty$) isotropic-nematic transition point. The axes are scaled by functions of α , $\tilde{\mu}_0(\alpha)$ and $A_0(\alpha)$, which can be found in Appendix C.

The U state contains an order parameter symmetry

$$S_y(x) = S_z(x) = -\frac{1}{2}S_x(x). \quad (4)$$

According to these only one order parameter is independent for a system at the U state.

To measure the biaxiality of B state, we define

$$P(x) \equiv S_y(x) - S_z(x). \quad (5)$$

The *uniaxial* phase, for example, is characterized by $P(x) = 0$ over the entire slit, and in the biaxial phase, nonvanishing P significantly develops only in the near-wall regions. The central region of the slit of U and B states has vanishing or weak orientational ordering.

Technically, the C phase is also biaxial, however, having a higher average density between the walls (see below). What distinguishes it from a P state is the strong orientational ordering of molecules in the central slit region. Here we have followed the terminology used in related studies^{17,19,21} and refer to the low-density biaxial phase as a biaxial phase and the high-density biaxial phase as a condensed phase.

1.3 Theoretical framework

In the current work, we focus on the physical properties of n semiflexible wormlike polymers confined between two flat surfaces separated by a distance H . Each polymer has length L and persistence length λ .^{26,33} Out of three length scales, only two reduced ones are relevant, H/L and $\alpha \equiv L/2\lambda$. The parameter α determines rigidity and flexibility of a polymer. A rodlike polymer, for example, is characterized by $\alpha \ll 1$ and flexible polymer by $\alpha \gg 1$. In a typical theoretical framework, the length scale λ disappears from the formalism after taking the $\alpha \ll 1$ asymptotic limit.

In a lyotropic liquid crystal system, another important parameter is the number density of polymer chains $\rho = n/V$ where V is the volume of the system. According to Onsager, the mutual exclusion of polymer segments that have a hard-core diameter d is the mechanism that drives the liquid-crystal formation in these systems. A high density drives the polymer segments to order orientationally.²⁸ In the current confinement system, the local density near the wall drives the surface orientational ordering to occur. Across the entire slit, we expect that the polymer density varies as a function of x . Instead of density, a convenient control parameter is the system chemical potential, μ , which is related to the bulk free energy F by

$$\mu = \frac{\partial F}{\partial n}. \quad (6)$$

Hence our phase diagram will be described by using H/L , α , and

$$\tilde{\mu} = \beta\mu. \quad (7)$$

The bulk isotropic state, for example, has a reduced chemical potential $\tilde{\mu}$ that is related to the reduced density $dL^2\rho$. The expression within a second-virial approximation can be found in Eq. (28). The chemical potential as a function of the reduced density has different branches, corresponding to different phases. In general, along the same branch, $\tilde{\mu}$ increases as a function of the reduced density.

A self-consistent field theory (SCFT) can be established to describe the free energy of this spatially inhomogeneous and orientationally ordered system by incorporating the Onsager interaction between polymer segments.²⁶ For consistency, in Appendix A, we present the major structure of the theory, which depends on three parameters, α , $H/2\lambda$, and $\tilde{\mu}$.

2 Rodlike particles in slit confinement, $\alpha = 0$

We first discuss the surface properties of an $\alpha = 0$ system (rodlike particles). The surface phase diagram is plotted in Fig. 3(A) in terms of $\tilde{\mu}/\tilde{\mu}_0(0)$ and $H/2\lambda A_0(\alpha)$ where $\tilde{\mu}_0(0) = 9.0132\dots$ and $A_0(\alpha) = \alpha$ are scaling factors listed in Appendix C. In the asymptotic $\alpha \ll 1$ limit, the combination $2\lambda A_0(\alpha) = L$ becomes λ -independent. There are three branches of the SCFT solution, corresponding to surface states with distinctively different symmetries as illustrated in Fig. 2: U, B, and C.

2.1 Uniaxial-biaxial phase transition

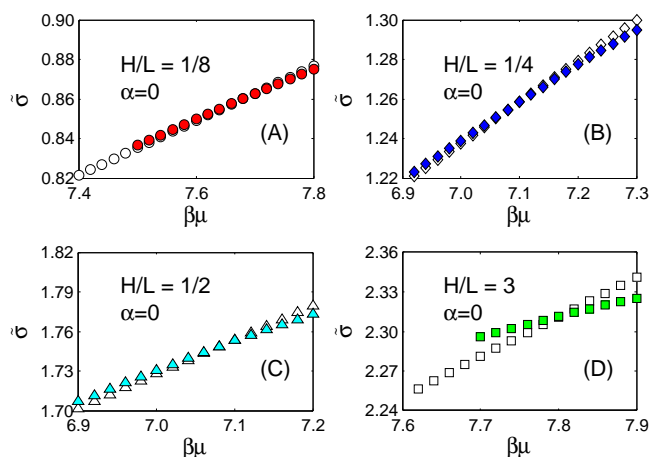


Fig. 4 Reduced surface tension $\tilde{\sigma}$, defined by (48), as functions of the reduced chemical potential $\tilde{\mu} = \beta\mu$, for the uniaxial (open symbols) and biaxial (filled symbols) states for rodlike molecules confined in slit of reduced width $H/L = 1/8, 1/4, 1/2$ and 3.0 , represented by circles, diamonds, triangles, and squares, respectively.

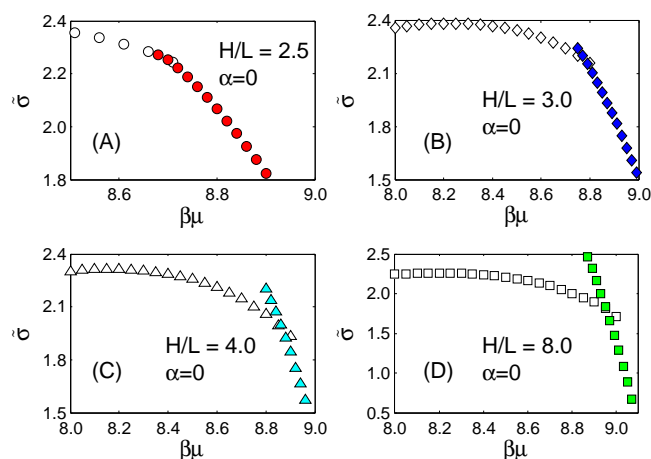


Fig. 5 Reduced surface tension $\tilde{\sigma}$ of the biaxial and condensed branches, corresponding to open and filled symbols, as functions of the reduced chemical potential $\tilde{\mu} = \beta\mu$ for a rodlike system $\alpha = 0$. Four examples are given here: $H/L = 2.5, 3.5, 4.0$, and 8.0 , represented by circles, diamonds, triangles, and squares.

To determine the U-B phase boundary, represented by symbols in the Fig. 3(A), for a given H/L we compare the reduced surface tension $\tilde{\sigma}$ of different states as a function of $\tilde{\mu}$. For example, in Fig. 4 we plot the numerical solution for both uniaxial and biaxial branches. In all cases, in particular high H/L cases, the two branches cross each other clearly, indicating a first-order phase transition. The uniaxial state is stable at low $\tilde{\mu}$ (low $\tilde{\rho}$ region) and the biaxial state is stable at high $\tilde{\mu}$ (high $\tilde{\rho}$ region).

The relative difference in slopes of the two surface-tension branches for a typical H/L in Fig. 4 becomes smaller, as H/L decreases. The first-order uniaxial-biaxial transition terminates at a second-order critical point at $H/L = 0$, labeled by a filled circle in Fig. 3(a). We project that at this point, $\tilde{\mu}/\tilde{\mu}_0(0) = 0.894\dots$, on the basis of an analysis from plots similar to those in Fig. 4, by reducing H/L consecutively.

2.2 Biaxial-condensed phase transition

In Fig. 5, we examine four examples of the reduced surface tension as a function of $\tilde{\mu}$ for given H/L . At relatively low $\tilde{\mu}$ (low $\tilde{\rho}$), the biaxial state is stable. At relatively high $\tilde{\mu}$ (high $\tilde{\rho}$) the condensed state has a lower free energy hence it is stable. The crossing point of the two typical curves determines the phase boundary, which is plotted by diamonds in Fig. 3(a). At the asymptotic limit $H/L \gg 1$, both states in the system become bulk phases: isotropic and nematic; in terms of the reduced chemical potential $\tilde{\mu}$, the transition then takes place at the bulk isotropic-nematic transition point $\tilde{\mu}_0$. This limit is indicated by an arrow in Fig. 3(a).

The first-order characteristic is weakened as the system ap-

proaches the critical point by lowering H/L . The entire first-order curve terminates at a critical point labeled by the filled diamond in Fig. 3(a).

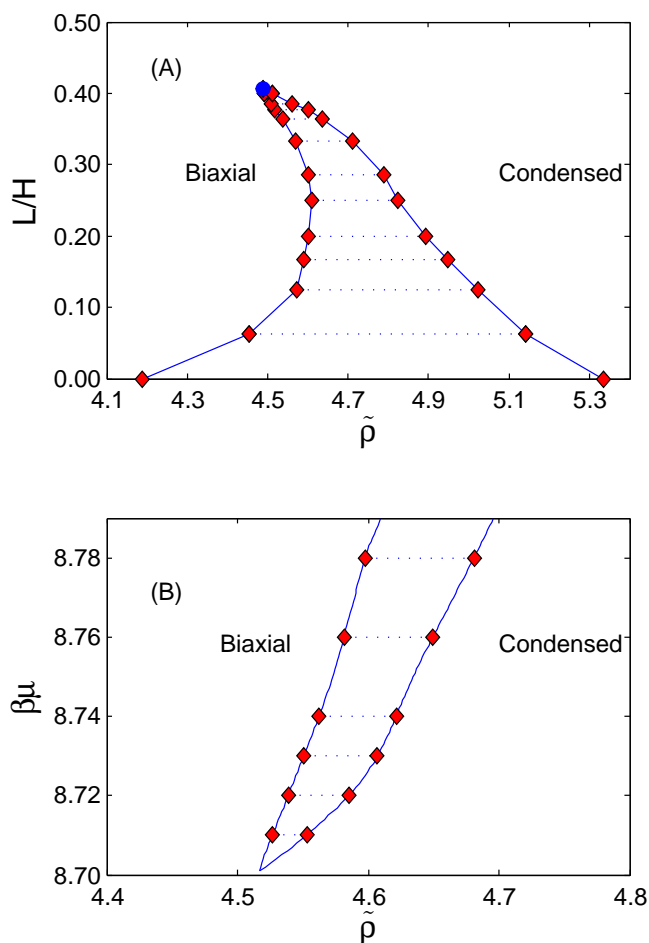


Fig. 6 Phase diagram of the biaxial-condensed transition in other perspectives: (a) $L/H - \tilde{\rho}$ diagram and (b) $\tilde{\mu} - \tilde{\rho}$ diagram. In both plots, the biaxial-condensed co-existence region is shown.

The B-C phase transition can be viewed in other representations. Figure 6 shows the phase diagram in $L/H - \tilde{\rho}$ view and $\tilde{\mu} - \tilde{\rho}$ view respectively. The middle portion of the diagrams are the coexistence region of biaxial and condensed states. These phase diagrams can be compared with the liquid-vapour phase transition diagram, where the density coexistence region is possible. The coexistence region terminates at a critical point.

The critical point [filled diamond in Fig.3 (A)] for the B-C transition, specified by μ_c and H_c/L , is determined by consideration of the the co-existence density difference in Fig. 6, represented by the magnitude of the dashed lines. Since we are dealing with a mean-field theory, we expect that the den-

sity difference follows the power law

$$\Delta\tilde{\rho} \propto (H - H_c)^{1/2} \quad (8)$$

as the critical point is approached in Fig. 6(A). Similarly we expect

$$\Delta\tilde{\rho} \propto (\tilde{\mu} - \tilde{\mu}_c)^{1/2} \quad (9)$$

in Fig. 6(B). A linear regression on the data of $[\Delta\tilde{\rho}]^2$ yields the critical values, $H_c/L = 2.46 \pm 0.1$ and $\tilde{\mu}_c = 8.7 \pm 0.1$ based on the current model.

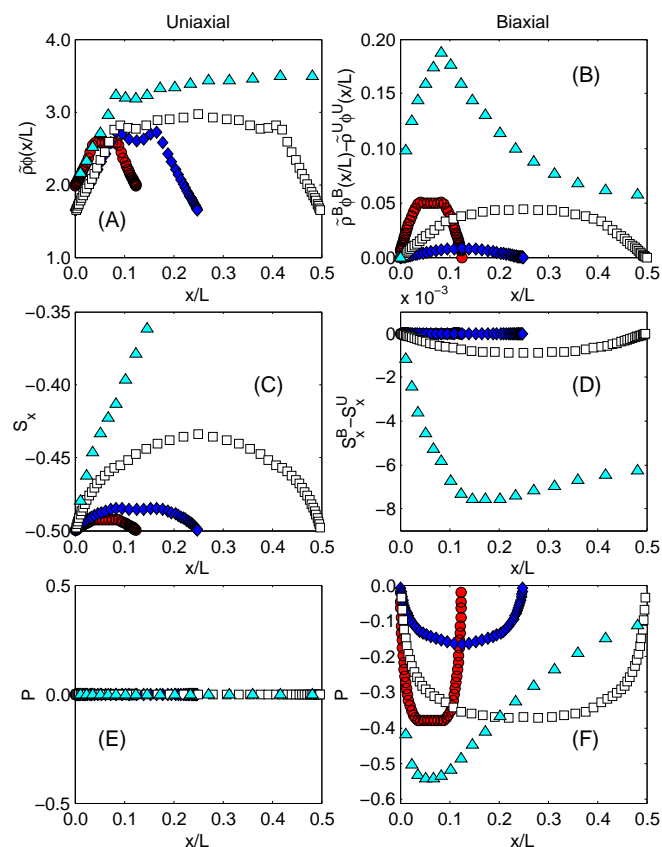


Fig. 7 Density and orientational order-parameter profiles for at the coexisting uniaxial (left) and biaxial (right) states at the uniaxial-biaxial transition point for $H/L = 1/8$ (circles), $1/4$ (diamonds), $1/2$ (squares), and 3 (triangles). At the these transition points, the reduced chemical potential has the value $\tilde{\mu} = 7.69, 7.12, 7.10,$ and $7.80,$ respectively. Only the portion near the left wall is displayed for the $H/L = 3.0$ case.

2.3 Density and orientational-order-parameter profiles

The variation of segmental density across the slit, after averaging over the orientational distributions, can be obtained

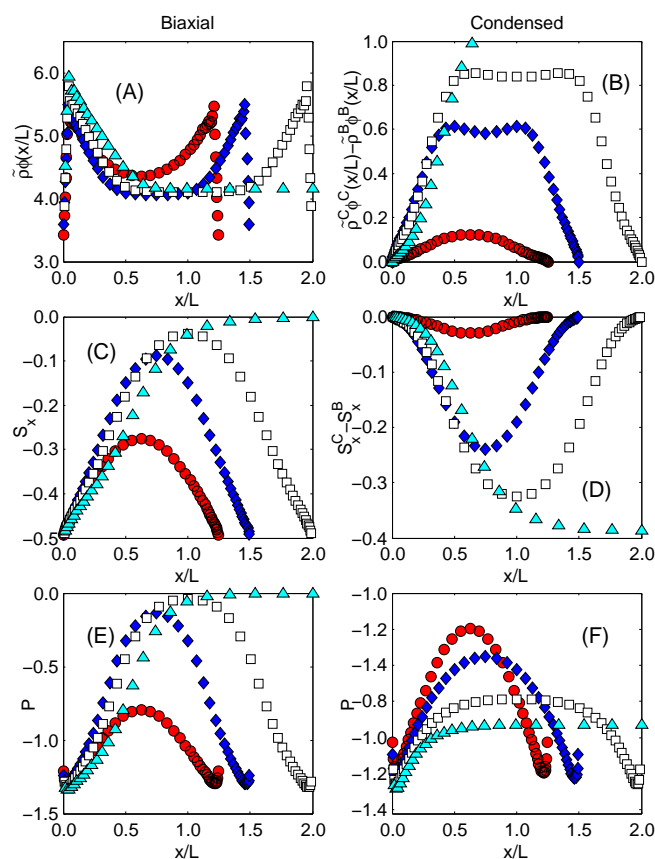


Fig. 8 Density and order parameter profiles of biaxial and condensed state at the B-C transition point, for $\alpha = 0$, the rod limit. $\tilde{H} = 2.5$ (circles), 3.0(diamonds), 4.0(squares), 8.0(triangles) are shown in this plot, corresponding to $\tilde{\mu} = 8.72, 8.78, 8.86, 8.95$, respectively.

from $\tilde{\rho}\Phi(\bar{x})$ where

$$\Phi(\bar{x}) = \int \phi(\bar{x}, \mathbf{u}) d\mathbf{u} \quad (10)$$

is the orientationally averaged density. Figures 7(a) and 7(b) show the density profiles at the uniaxial-biaxial transition point for a selection of H/L at 1/8, 1/4, 1/2 and 3. Figures 8(a) and 8(b) show the density profiles at the biaxial-condensed transition point for a selection of H/L at 2.5, 3.0, 4.0 and 8.0. The two (b) plots of the figures display the density difference for a clearer presentation.

One significant feature is the cusplike shape near the wall. This mirrors the density profile of a dilute rodlike molecule solution near a single wall, studied by Poniewierski, who also found a similar singularity on the center-of-mass density profile near the wall, at approximately $x/L = 1/2$.³⁴ In this paper, we used a contour-based density function rather than the center-of-mass density. The two physical quantities are related

to each other by a transformation that integrates over the path variable.²⁶ Transforming Φ back to the center-of-mass density profile, we found that the cusp occurs at the same $x/L = 1/2$ location.

The order parameter profile $S_x(x)$ and biaxiality profile $P(x)$, defined in (2) and (5), are displayed in Fig. 7(c)-(f) as well as Fig. 8(c)-(f). As $\tilde{\mu}$ increases, the density near the wall is significantly larger in comparison with the density at the slit center. Due to the large density enhancement, $S_z(x)$ is positively large at the places where $\Phi(x)$ is large. This causes the large negative value of P in plots 7(f) and 8(f). Note that over the entire x/L , $P(x)$ in Fig. 7(e) is identically zero, which reflects the symmetry of the uniaxial phase. In $H/L \gg 1$ systems, the central region of the slit of the B state has a P value close to 0 as well, which is a reminiscent of the bulk isotropic phase. In $H/L \sim 1$ systems, at the U-C transition, the C state displays even more biaxiality over the entire region, in comparison with the B state.

3 The case of $\alpha \neq 0$, semiflexible chains in slit confinement

3.1 Phase Diagram of flexible wormlike chains $\alpha \gg 1$

In the asymptotic $L \gg 2\lambda$ limit, we can already guess the qualitative phase diagram by working on a scaling analysis. The dominant length scale is the effective Kuhn length $a = 2\lambda$. The total chain length L , which is an important length scale in rodlike molecular system, now plays a role of providing L/a persistent segments so that the total effective rigid segments in the system is $n_{\text{eff}} = nL/a$. Taking $L_{\text{eff}} = a$ as the new basic length scale of the effective rodlike segments, we can deduce the scaling behavior of the bulk isotropic-nematic transition density. The Onsager interaction coefficient, for example, becomes $L_{\text{eff}}^2 d$ instead of $L^2 d$. Hence the isotropic-nematic transition occurs at a reduced density $n_{\text{eff}} L_{\text{eff}}^2 d / V \sim nLa^{-1} a^2 d / V = nLad / V$. The effective chemical potential at the transition point becomes $(\partial F / \partial n)_{\text{eff}} = (L/a)^{-1} \mu$. Hence, if we qualitatively map the phase diagram in Fig. 3(a) to Fig. 3(e), μ_0 on the vertical axis, i.e., the transition chemical potential $\tilde{\mu}_0$, is proportional to L/a . Because the effective length is $L_{\text{eff}} = a$, the horizontal axis should be replaced by $H/L_{\text{eff}} = H/a$. The qualitative feature then remains the same as Fig. 3(a).

Indeed, a SCFT-based precise calculation of the $\alpha \gg 1$ case gives rise to Fig. 3(e), where all these scaling properties are preserved. The transition chemical potential, for example, has the value $\tilde{\mu}_0 = (20.498\dots)L/a$ and the bulk isotropic-nematic transition occurs at $\tilde{\rho}^1 = (13.0495\dots)a/L$ and $\tilde{\rho}^N = (14.0769\dots)a/L$.²⁹ Our phase diagram for the $\alpha \gg 1$ case in Fig. 3(d) is identical to the one calculated for the same system but with a different numerical approach in Ref. [21]. The read-

ers are referred to this reference for more detailed description of the structural properties.

3.2 Phase Diagram of wormlike chains: other α

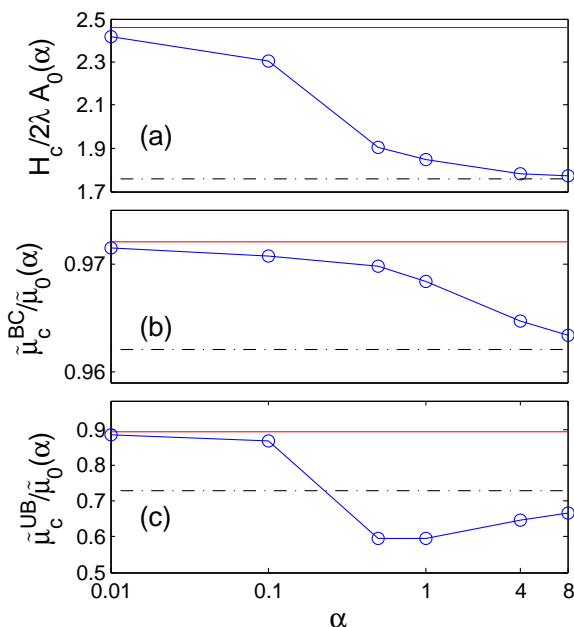


Fig. 9 The location of the two critical points as a function of the flexibility α . The U-B critical point is located at $H_c = 0$ and $\tilde{\mu}_c^{\text{UB}}$ shown by the line behind circles in plot (c). The B-C critical point is located at H_c shown by the line behind circles in plot (a), and $\tilde{\mu}_c^{\text{BC}}$ shown by the line behind circles in plot (b). Solid and dashed lines indicate the asymptotic values at $\alpha = 0$ (left) and $\alpha = \infty$ (right).

For other values of α , we expect a crossover of the phase diagrams from Fig. 3(a) to Fig. 3(e). Three intermediate cases are plotted as (b) [for $\alpha = 0.1$], (c) [for $\alpha = 1$], and (d) [for $\alpha = 4$] in this figure. To facilitate the plots within a reasonable scale, we reduce the vertical axis by $\tilde{\mu}_0(\alpha)$ and use the Kratky-Porod factor $A_0(\alpha)$ defined in Appendix C to scale the horizontal axis so that the crossover from H/L to H/a can be maintained within a similar scale.

The main structure of the phase diagram, the first-order nature of the U-B and B-C phase transitions and the existence of two critical points on the phase diagram, remains the same. In Figs. 9(a) and (b), we plot the location of the critical point, in terms of H_c and $\tilde{\mu}_c^{\text{BC}}$, as a function of α for the B-C transition. In Fig. 9(c), we plot the location of the critical point, in terms of $\tilde{\mu}_c^{\text{UB}}$, happening at $H_c = 0$, as a function of α for the U-B transition.

4 Uniaxial-biaxial phase transition: first-order vs. second-order

The numerical evidence of the crossing of two branches (U and B) of the free energy in Fig. 4, in particular at large H/L indicates the first-order nature of the U-B transition. Similar numerical results were found in Ref. 21, based on a different numerical technique. This is produced from the same SCFT where both angular dependence and positional dependence of the distribution function varies continuously.

The numerical solution based on the Zwanzig model for rodlike molecules, however, indicated a different story. The U-B transition line, for example, was found to be a flat, second-order line in parallel to the H/L axis, which can be contrasted with the variation of the first-order U-B boundary as a function of H in the current work. Although the interaction form expressed in (13) appears to be local, it has a nonlocal nature from the perspective of the rod-center-to-rod-center interaction. This can be rigorously shown by transforming the quantities in the free energy, (12), to new notations that use a density distribution function based on the center of mass of a rod molecule.^{26,35} It is unlikely that the difference between the results yielded from the two models is caused by how the excluded-volume interaction is handled. Within the Zwanzig model, only three representative orientational directions, along the three main axes are allowed. A rod molecule is allowed to point in these three directions only. Hence the orientational dependence is oversimplified in Refs. 17, 19. This is more likely the reason that has caused the difference.

Recent Monte Carlo simulations of semiflexible polymers with excluded-volume interactions produced a similar μ - H phase diagram.²³⁻²⁵ Many features on the phase diagrams are similar, including the bending of both μ - H boundaries to lower μ values as H reduces (however, the μ - H curve of the U-B transition was projected to be flat in Ref. 23). In the earlier work, the biaxiality versus chemical potential plot in Fig. 7(b) of Ref. 23, for example, displays a seemingly finite jump at the U-B transition. This apparent first-order signature was later dismissed by the same authors and a second-order U-B transition scenario was proposed.^{23,25,36} A discrepancy regarding the order of the U-B transition exists between these Monte Carlo simulations and the current SCFT results. It is unclear whether the discrepancy can be attributed to the finite lattice setting used in the simulations.

Strictly speaking, a direct comparison between our results on a lyotropic system and those on a thermotropic system cannot be made. It is, however, worthwhile to note that lowering temperature in a thermotropic system encourage stronger nematic ordering. This has the same effect as in a lyotropic system when the chemical potential increases. The two staged transitions, U-B and B-C, can be compared with the surface nematic and bulk nematic transition observed recently in a

thermotropic system. Aya *et al.* The observed heat capacity curve associated with the surface transition has a sharp peak, characteristic of a first-order transition. The experiment observation was explained by a Maier-Saupe theory based on a structure similar to a typical Onsager theory for a lyotropic system — here we must effectively regard the Maier-Saupe coefficient as a function of density. The two staged transitions found in this theoretical work also predicted a first-order surface transition, consistent with what we see here on the U-B transition.

A definitive examination of the order of the U-B transition within the current SCFT would be to conduct a simultaneous expansion of the free energy expression in (39) as a function of S_x and P . The first step is the expansion of the mean-field W in terms of spherical harmonics, where two order parameters, representing the biaxial and main orientational ordering, show up in the second-rank spherical harmonics. The modified diffusion equation can then be solved based on a similar expansion of the propagator function. Through (43), a connection can be established between these field-based order parameters and S_x and P . At this stage, the free energy is expanded in S_x and P . Note that (42) should not be used in this process (i.e., the free energy is not yet minimized as a function of ϕ). The end result is a Landau-type free energy expansion, which can be minimized with respect to S_x and P and allows the identification of the transition order through an analysis of the leading terms. This procedure was used for analytically calculating the bulk isotropic-nematic transition of a two-dimensional system, which is a much simpler case.³⁷

5 Summary

In summary, the confinement of semi-flexible polymer chains is studied with the inclusion of the Onsager excluded-volume interaction, for various degrees of flexibility, ranging from 0 to ∞ . We have also shown that three surface phases, uniaxial, biaxial, and condensed, can exist in this system, depending on the magnitude of the slit width and average density within the slit.

References

- 1 P. Sheng, *Phys. Rev. Lett.*, 1976, **37**, 1059–1062.
- 2 P. Sheng, *Phys. Rev. A*, 1982, **26**, 1610–1617.
- 3 T. J. Sluckin and A. Poniewierski, *Phys. Rev. Lett.*, 1985, **55**, 2907–2910.
- 4 A. Poniewierski and T. J. Sluckin, *Liquid Crystals*, 1987, **2**, 281–311.
- 5 A. K. Sen and D. E. Sullivan, *Phys. Rev. A*, 1987, **35**, 1391–1403.
- 6 I. Rodríguez-Ponce, J. M. Romero-Enrique, E. Velasco, L. Mederos and L. F. Rull, *Phys. Rev. Lett.*, 1999, **82**, 2697–2700.
- 7 A. V. Emelyanenko, S. Aya, Y. Sasaki, F. Araoka, K. Ema, K. Ishikawa and H. Takezoe, *Phys. Rev. E*, 2011, **84**, 041701.
- 8 S. Aya, Y. Sasaki, F. Araoka, K. Ema, K. Ishikawa, A. V. Emelyanenko and H. Takezoe, *Phys. Rev. Lett.*, 2011, **106**, 117801.
- 9 A. B. G. M. Leferink op Reinink, E. van den Pol, A. V. Petukhov, G. J. Vroege and H. N. W. Lekkerkerker, *The European Physical Journal Special Topics*, 2013, **222**, 3053–3069.
- 10 Z. Y. Chen and S.-M. Cui, *Phys. Rev. E*, 1995, **52**, 3876–3880.
- 11 L. Harnau and S. Dietrich, *Phys. Rev. E*, 2002, **66**, 051702.
- 12 K. Shundyak and R. van Roij, *Europhys. Lett.*, 2006, **74**, 1039.
- 13 M. Dijkstra, R. van Roij and R. Evans, *Phys. Rev. E*, 2001, **63**, 051703.
- 14 A. Chrzanowska, P. I. C. Teixeira, H. Ehrentraut and D. J. Cleaver, *Journal of Physics: Condensed Matter*, 2001, **13**, 4715.
- 15 A. Chrzanowska, *Journal of Computational Physics*, 2003, **191**, 265 – 281.
- 16 D. de las Heras, E. Velasco and L. Mederos, *The Journal of Chemical Physics*, 2004, **120**, 4949–4957.
- 17 R. van Roij, M. Dijkstra and R. Evans, *Europhys. Lett.*, 2000, **49**, 350–356.
- 18 R. Zwanzig, *The Journal of Chemical Physics*, 1963, **39**, 1714–1721.
- 19 R. van Roij, M. Dijkstra and R. Evans, *The Journal of Chemical Physics*, 2000, **113**, 7689–7701.
- 20 J. Z. Y. Chen, D. E. Sullivan and X. Yuan, *Europhys. Lett.*, 2005, **72**, 89.
- 21 J. Z. Y. Chen, D. E. Sullivan and X. Yuan, *Macromolecules*, 2007, **40**, 1187–1195.
- 22 H. Steuer, S. Hess and M. Schoen, *Phys. Rev. E*, 2004, **69**, 031708.
- 23 V. A. Ivanov, A. S. Rodionova, E. A. An, J. A. Martemyanova, M. R. Stukan, M. Müller, W. Paul and K. Binder, *Phys. Rev. E*, 2011, **84**, 041810.
- 24 V. A. Ivanov, A. S. Rodionova, J. A. Martemyanova, M. R. Stukan, M. Müller, W. Paul and K. Binder, *The Journal of Chemical Physics*, 2013, **138**, 234903.
- 25 V. A. Ivanov, A. S. Rodionova, J. A. Martemyanova, M. R. Stukan, M. Müller, W. Paul and K. Binder, *Macromolecules*, 2014, **47**, 1206–1220.
- 26 J. Z. Y. Chen, *Prog. Polym. Sci.*, 2016, **00**, doi:10.1016/j.progpolymsci.2015.09.002.

- 27 A. Khokhlov and A. Semenov, *Phys. A*, 1982, **112**, 605–614.
- 28 L. Onsager, *Ann. N. Y. Acad. Sci.*, 1949, **51**, 627–659.
- 29 Z. Y. Chen, *Macromolecules*, 1993, **26**, 3419–3423.
- 30 Z. Y. Chen, *Phys. Rev. E*, 1993, **47**, 3765–3767.
- 31 Y. Jiang and J. Z. Y. Chen, *Macromolecules*, 2010, **43**, 10668–10678.
- 32 P. G. de Gennes and J. Prost, *The Physics of Liquid Crystals*, 2nd ed., Clarendon Press, Oxford, 1993.
- 33 N. Saito, K. Takahashi and Y. Yunoki, *J. Phys. Soc. Jpn*, 1967, **22**, 219.
- 34 A. Poniewierski, *Phys. Rev. E*, 1993, **47**, 3396–3403.
- 35 J. Z. Y. Chen, *Soft Matter*, 2013, **9**, 10921.
- 36 V. A. Ivanov, J. A. Martemyanova, A. S. Rodionova and M. R. Stukan, *Polymer Science Series C*, 2013, **55**, 4–22.
- 37 Z. Y. Chen, *Phys. Rev. Lett.*, 1993, **71**, 93–96.
- 38 M. Doi and S. F. Edwards, *The Theory of Polymer Dynamics*, Oxford University Press, New York, 1988.
- 39 G. H. Fredrickson, *The equilibrium theory of inhomogeneous polymers*, Clarendon Press, Oxford, 2006.
- 40 T. Odijk, *Macromolecules*, 1986, **19**, 2313–2329.
- 41 G. J. Vroege and T. Odijk, *Macromolecules*, 1988, **21**, 2848–2858.
- 42 R. J. LeVeque, *Finite Volume Methods for Hyperbolic Problems*, Cambridge University Press, 2002.

A SCFT for wormlike polymers

We consider a system of volume V consisting of n wormlike homopolymers confined between two parallel flat plates separated by a distance H . The overall chain density is hence $\rho_0 = n/V$. Every polymer chain is modeled by a cylindrical filament which has total a contour length L , diameter d , and persistence length λ .^{33,38} A coordinate system is displayed in Fig. 1, together with a representative chain.

Let $\rho(\mathbf{r}, \mathbf{u})$ be the probability distribution function of finding a segment of the polymer chain located at \mathbf{r} and pointing in the tangential direction \mathbf{u} , such that

$$\int d\mathbf{r} d\mathbf{u} \rho(\mathbf{r}, \mathbf{u}) = n. \quad (11)$$

Within the self-consistent field theory in which a mean field $W(\mathbf{r}, \mathbf{u})$ coupled with $\rho(\mathbf{r}, \mathbf{u})$ is introduced, the system free energy, F , can be written as²⁶

$$\beta F = n \ln(n/Q) + n \ln C_0 - \int d\mathbf{r} d\mathbf{u} W(\mathbf{r}, \mathbf{u}) \rho(\mathbf{r}, \mathbf{u}) + \frac{1}{2} \int d\mathbf{r} d\mathbf{u} \int d\mathbf{r}' d\mathbf{u}' \rho(\mathbf{r}, \mathbf{u}) V(\mathbf{r}, \mathbf{u}; \mathbf{r}', \mathbf{u}') \rho(\mathbf{r}', \mathbf{u}') \quad (12)$$

where $\beta = 1/k_B T$ with k_B as the Boltzmann constant and T temperature. The free-energy constant C_0 is set at $C_0 = 4\pi dL^2$

for below convenience. The expression is accurate at the level of second-virial approximation. According to Onsager's original idea of rod-rod interaction,²⁸ one can rigorously express the Mayer function V in the last term to represent the orientationally dependent polymer segment-segment interaction

$$V(\mathbf{r}, \mathbf{u}; \mathbf{r}', \mathbf{u}') = 2dL^2 \delta(\mathbf{r} - \mathbf{r}') |\mathbf{u} \times \mathbf{u}'|, \quad (13)$$

which was first introduced for wormlike chains by Khokhlov and Semenov.²⁷

We remark on the use of the apparently local interaction energy in the above expression. Such an expression is used together with the contour-averaged density distribution $\rho(\mathbf{r}, \mathbf{u})$, which is different from the density function defined based on the properties at the center of mass $\rho_c(\mathbf{r}, \mathbf{u})$. This is a particularly important point, as within the $\alpha = 0$ limit, these two distribution functions are different in a spatially inhomogeneous system; the use of $\rho_c(\mathbf{r}, \mathbf{u})$, for example, requires a nonlocal Onsager interaction energy. The transformation of the formalism, from using $\rho(\mathbf{r}, \mathbf{u})$ and the local interaction energy, to using $\rho_c(\mathbf{r}, \mathbf{u})$ and a nonlocal interaction energy, can be found in Refs. 26, 35.

The single-chain partition function in an external field $W(\mathbf{r}, \mathbf{u})$, Q , can be calculated from

$$Q = \int d\mathbf{r} d\mathbf{u} q(\mathbf{r}, \mathbf{u}; 1), \quad (14)$$

where $q(\mathbf{r}, \mathbf{u}; t)$ is the propagator used in polymer theory to represent the probability of finding a polymer segment of chain length Lt , whose t -terminal end is located at the position \mathbf{r} and points to the direction of \mathbf{u} .^{26,39} The propagator can be calculated from solving a modified diffusion equation,

$$\frac{\partial}{\partial t} q(\mathbf{r}, \mathbf{u}; t) = \left[\frac{L}{2\lambda} \nabla_{\mathbf{u}}^2 - L\mathbf{u} \cdot \nabla_{\mathbf{r}} - W(\mathbf{r}, \mathbf{u}) \right] q(\mathbf{r}, \mathbf{u}; t), \quad (15)$$

provided an initial condition $q(\mathbf{r}, \mathbf{u}; 0) = 1$. The entire theoretical framework needs two more relationships for self-consistency. Minimizing F with respect to ρ yields

$$W(\mathbf{r}, \mathbf{u}) = 2dL^2 \int d\mathbf{u}' |\mathbf{u} \times \mathbf{u}'| \rho(\mathbf{r}, \mathbf{u}'), \quad (16)$$

and minimizing F with respect to W yields

$$\rho(\mathbf{r}, \mathbf{u}) = \frac{n}{Q} \int_0^1 dt q(\mathbf{r}, \mathbf{u}; t) q(\mathbf{r}, -\mathbf{u}; 1-t). \quad (17)$$

We need to solve the coupled integrodifferential Eqs. (14)-(17) for the current problem.

To proceed further we define a dimensionless density

$$\tilde{\rho} = dL^2 \rho_0 \quad (18)$$

and a dimensionless probability,

$$\phi(\mathbf{r}, \mathbf{u}) \equiv \rho(\mathbf{r}, \mathbf{u}) / \rho_0, \quad (19)$$

the fraction of polymer segments in a chain that is located at \mathbf{r} and points to the direction of \mathbf{u} . The latter obeys the normalization condition

$$\frac{1}{V} \int d\mathbf{r} d\mathbf{u} \phi(\mathbf{r}, \mathbf{u}) = 1. \quad (20)$$

B Homogeneous bulk phases

The problem at hand is the calculation of the probability distribution function which depends on the overall density ρ_0 of the system. Here we review the main bulk properties of the isotropic-nematic transition resulted from solving the above theory.^{27,29,40,41}

As all \mathbf{r} dependence for the homogeneous bulk property is removed, the only variable becomes \mathbf{u} in the theory. Adding a subscript b (bulk) to all quantities, we rewrite the free energy per chain as

$$\begin{aligned} \frac{\beta F_b}{n} = & \ln \left(\frac{4\pi\tilde{\rho}}{Q/V} \right) - \int d\mathbf{u} W_b(\mathbf{u}) \phi_b(\mathbf{u}) \\ & + \tilde{\rho} \int d\mathbf{u} \int d\mathbf{u}' \phi_b(\mathbf{u}) |\mathbf{u} \times \mathbf{u}'| \phi_b(\mathbf{u}') \end{aligned} \quad (21)$$

where $\int d\mathbf{u} \phi_b(\mathbf{u}) = 1$. There are two parameters in the model.

- The reduced density $\tilde{\rho}$ which appears in the free energy expression above, and the resulting mean field in (16).
- The ratio

$$\alpha \equiv L/2\lambda \quad (22)$$

that appears in the first term on the right-hand side of MDE in Eq. (15). The second, coupling term vanishes for the bulk problem. The parameter α determines the flexibility of the wormlike chain. In the limit $\alpha \ll 1$, we recover the original Onsager theory for rods,^{28,40} and in the limit $\alpha \gg 1$, we recover the Khokhlov-Semenov theory for flexible chains.^{27,40}

Once the self-consistent set of equations, Eqs. (14)-(17), are solve for given $\tilde{\rho}$ and α , the free energy as a function of density is known.^{29,31} We can then calculate the chemical potential

$$\mu \equiv \left[\frac{\partial F}{\partial n} \right]_{T,V}$$

and the osmotic pressure

$$P \equiv - \left[\frac{\partial F}{\partial V} \right]_{T,n}$$

for the bulk system. The reduced versions are

$$\tilde{\mu} \equiv \tilde{\mu} = 1 + \ln \left(\frac{4\pi\tilde{\rho}}{Q/V} \right), \quad (23)$$

and

$$\tilde{P} \equiv \beta P dL^2 = \tilde{\rho} + \tilde{\rho}^2 \int d\mathbf{u} d\mathbf{u}' \phi_b(\mathbf{u}) |\mathbf{u} \times \mathbf{u}'| \phi_b(\mathbf{u}'). \quad (24)$$

In particular, for the orientationally isotropic (i) phase, we can show

$$W_b^i(\mathbf{u}) = \tilde{\rho}^i \pi/2. \quad (25)$$

The partial differential equation in (15) has a trivial solution,

$$q_b^i(\mathbf{u}; t) = \exp(-\pi\tilde{\rho}^i t/2). \quad (26)$$

Using that we arrive at the free energy for the isotropic state

$$\frac{\beta F^i}{n} = \ln(\tilde{\rho}^i) + \frac{\pi\tilde{\rho}^i}{4}. \quad (27)$$

Hence, for the isotropic state the reduced chemical potential and pressure are

$$\tilde{\mu}^i = 1 + \ln(\tilde{\rho}^i) + \pi\tilde{\rho}^i/2. \quad (28)$$

and

$$\tilde{P}^i = \tilde{\rho}^i + \pi(\tilde{\rho}^i)^2/4. \quad (29)$$

These analytic expression are independent of the flexibility $L/2\lambda$. However, at the isotropic-nematic transition point, the transition density is dependent on $L/2\lambda$.

The system undergoes a first-order isotropic-nematic phase transition as $\tilde{\rho}$ increases. The densities of the isotropic and nematic phases at the transition, $\tilde{\rho}^i$ and $\tilde{\rho}^n$, can be determined from^{29,40}

$$\tilde{\mu}^i(\tilde{\rho}^i) = \tilde{\mu}^n(\tilde{\rho}^n) \quad (30)$$

and

$$\tilde{P}^i(\tilde{\rho}^i) = \tilde{P}^n(\tilde{\rho}^n). \quad (31)$$

where the quantities with a superscript n represent the nematic branch. The numerical results for the transition densities, $\tilde{\rho}^i$ and $\tilde{\rho}^n$, as a function of α are available in Ref. 29 and listed here in Appendix C.

C Previous results used in the text

Transition densities – Calculated in Ref. 29, the isotropic-nematic transition densities of the current model for the bulk phase are well represented by the empirical formula,

$$\tilde{\rho}_b^i(\alpha) = \frac{\sum_{j=0}^3 a_j(\alpha)^j}{1 + \sum_{j=1}^2 b_j(\alpha)^j} \quad (32)$$

$$\tilde{\rho}_b^n/\tilde{\rho}_b^i - 1 = \frac{\sum_{j=0}^3 a_j(\alpha)^j}{1 + \sum_{j=1}^3 b_j(\alpha)^j} \quad (33)$$

The coefficients a_j and b_j are listed in Table 2.

	a_0	a_1	a_2	a_3
ρ_b^i	4.1895	26.102	66.003	117.85
$\rho_b^n/\rho_b^i - 1$	0.2737	3.0357	3.0666	10.786
		b_1	b_2	b_3
ρ_b^i		3.4806	9.0331	0
$\rho_b^n/\rho_b^i - 1$		26.826	86.79	143.15

Table 2 Numerical coefficients in (32) and (33)

Reduced chemical potential – At the isotropic-nematic transition, according to the model in the text, the chemical potential has the value

$$\tilde{\mu}_0(\alpha) = 1 + \ln(\tilde{\rho}_b^i) + \pi\tilde{\rho}_b^i/2 \quad (34)$$

which is used for rescaling the vertical axis, $\tilde{\mu}$, in Fig. 3. The chemical potential has the asymptotic limits

$$\tilde{\mu}_0(\alpha) = \begin{cases} 9.0132\dots, & \text{when } \alpha \ll 1, \\ \alpha \times 20.498\dots, & \text{when } \alpha \gg 1. \end{cases} \quad (35)$$

Kratky-Porod factor – In the text, we use a scaling factor $A_0(\alpha)$ which is given by

$$A_0(\alpha) = [2\alpha + \exp(-2\alpha) - 1]/2\alpha. \quad (36)$$

The Kratky-Porod expression for the mean square end-to-end distance is related to the above by $\langle R^2 \rangle = 2\lambda LA_0(\alpha)$. The Kratky-Porod factor $A_0(\alpha)$ has the asymptotic limits

$$A_0(\alpha) = \begin{cases} \alpha, & \text{when } \alpha \ll 1, \\ 1, & \text{when } \alpha \gg 1. \end{cases} \quad (37)$$

D Reduced theory for slit confinement

The basic assumption is that the segment density of system is uniform in both y - and z - directions and has variation in x only [see Fig. 1]. Using the slit width H as the basic unit, the reduced variable

$$\tilde{x} = x/H \quad (38)$$

has a range $[0, 1]$ where H is the slit width. We can show that the free energy can be rewritten as

$$\begin{aligned} \frac{\beta F}{n} = & \ln\left(\frac{4\pi\tilde{\rho}}{\tilde{Q}}\right) - \int_0^1 d\tilde{x} \int d\mathbf{u} W(\tilde{x}, \mathbf{u}) \phi(\tilde{x}, \mathbf{u}) \\ & + \tilde{\rho} \int_0^1 d\tilde{x} \int d\mathbf{u} d\mathbf{u}' \phi(\tilde{x}, \mathbf{u}) |\mathbf{u} \times \mathbf{u}'| \phi(\tilde{x}, \mathbf{u}') \end{aligned} \quad (39)$$

where

$$\tilde{Q} \equiv \int_0^1 d\tilde{x} \int d\mathbf{u} q(\tilde{x}, \mathbf{u}; 1). \quad (40)$$

The propagator q now satisfies

$$\frac{\partial}{\partial t} q(\tilde{x}, \mathbf{u}; t) = \left[\frac{L}{2\lambda} \nabla_{\mathbf{u}}^2 - \frac{L}{H} u_x \frac{d}{d\tilde{x}} - W(\tilde{x}, \mathbf{u}) \right] q(\tilde{x}, \mathbf{u}; t). \quad (41)$$

where $u_x = \mathbf{u} \cdot \hat{x}$. Equations (16) and (17) become

$$W(\tilde{x}, \mathbf{u}) = 2\tilde{\rho} \int d\mathbf{u}' |\mathbf{u} \times \mathbf{u}'| \phi(\tilde{x}, \mathbf{u}'), \quad (42)$$

and

$$\phi(\tilde{x}, \mathbf{u}) = \frac{1}{\tilde{Q}} \int_0^1 dt q(\tilde{x}, \mathbf{u}; t) q(\tilde{x}, -\mathbf{u}; 1-t). \quad (43)$$

The hard-wall boundary conditions needed for solving (41) are given as²⁶,

$$\begin{cases} q(0, \mathbf{u}; t) = 0, & \text{if } u_x > 0 \text{ and } t \neq 0, \\ q(1, \mathbf{u}; t) = 0, & \text{if } u_x < 0 \text{ and } t \neq 0. \end{cases} \quad (44)$$

With the initial condition,

$$q(\tilde{x}, \mathbf{u}; 0) = \begin{cases} 0 & \text{if } u_x > 0 \text{ and } \tilde{x} = 0, \text{ or } u_x < 0 \text{ and } \tilde{x} = 1 \\ 1 & \text{otherwise,} \end{cases} \quad (45)$$

The above equations form the basic SCFT for the current slit system.

Taking derivatives of the free energy, we can show that the reduced chemical potential follow the same formal expression,

$$\tilde{\mu}(\tilde{\rho}) = 1 + \ln\left(\frac{4\pi\tilde{\rho}}{\tilde{Q}}\right) \quad (46)$$

where the minimization condition in (42) is assumed. Note \tilde{Q} depends on $\tilde{\rho}$ as well. The entire theory contains three basic parameters.

- The ratio $\alpha \equiv L/2\lambda$ defined in Eq. (22) and appears in (41) representing the flexibility of polymers.
- The ratio H/L appears in Eq. (41), representing the relative slit width. This parameter is new to the slit-confinement system. For the bulk phase $H/L = \infty$; the formalism returns to the one in Sect. B.
- The reduced density $\tilde{\rho}$. As it turns out, three surface states are possible. To study the first-order phase transitions between these phases, it is more convenient to directly use $\tilde{\mu}$ in (46) instead of $\tilde{\rho}$. Each state forms a unique $\tilde{\mu}$ - $\tilde{\rho}$ relationship.

For a slit with width ratio H/L , the Gibbs free energy of the system, G , is obtained from

$$G(H/L) \equiv F - \mu n \quad (47)$$

The determination of the stability of a surface state relies on a comparison of the surface tension σ , i.e., the Gibbs free energy difference per unit area of the slit wall. In reduced form,

$$\begin{aligned}\bar{\sigma}(\bar{\mu}) &\equiv (\beta dL^2/H)\sigma = (\beta dL^2/H)[G(H/L) - G(\infty)] \\ &= -\bar{\rho} - \bar{\rho}^2 \int_0^1 d\bar{x} d\mathbf{u} d\mathbf{u}' \phi(\bar{x}, \mathbf{u}) |\mathbf{u} \times \mathbf{u}'| \phi(\bar{x}, \mathbf{u}') \\ &\quad + \bar{\rho}^i + \frac{\pi}{4}(\bar{\rho}^i)^2\end{aligned}\quad (48)$$

where $\bar{\rho}$ is related to $\bar{\mu}$ by (46) and $\bar{\rho}^i$ is related to $\bar{\mu}$ by $\bar{\mu} = 1 + \ln(\bar{\rho}^i) + \pi\bar{\rho}^i/2$. We only consider the system with a bulk density up to the isotropic-nematic transition density.

E Numerical Methods

Main steps. – Three basic parameters α , H/L and $\bar{\mu}$ control the structure of the system. The numerical procedure used to solve SCFT in this work was of five major steps :

- An initial guess for $W(\bar{x}, \mathbf{u})$ is made. A more efficient method is to adopt an initial guess from an already converged function from a neighboring parameter point.
- The modified diffusion equation (MDE), Eq. (41), is solved with the consideration of the boundary conditions in Eq. (44) and initial condition condition in Eq. (45), for the propagator $q(\bar{x}, \mathbf{u}, t)$. For a given W function, the numerical algorithm of solving MDE follows the detailed steps outlined below.
- From the propagator we deduce the partition function \tilde{Q} from Eq. (40). From the relationship in Eq. (46) we estimate the average system density $\bar{\rho}$ on the basis of calculated \tilde{Q} and specified $\bar{\mu}$.
- The distribution density $\phi(\bar{x}, \mathbf{u})$ is then calculated based on Eq. (43).
- The SCFT field $W(\bar{x}, \mathbf{u})$ is updated by using Eq. (42).
- Steps (b)-(e) are repeated, now with a new W from step (e) as the initial guess. The entire procedure is considered convergent following the tolerance criterion — the maximum difference between the two W functions in (a) and (e) is less than 5×10^{-4} .

Solving MDE. – To solve MDE within step (b), we use the second order beam-warming scheme to deal with the advection part $\mathbf{u} \cdot \nabla q(\bar{x}, \mathbf{u}, t)$ in the equation.⁴² The range for \bar{x} is divided into N_x points. The vector \mathbf{u} is represented by spherical coordinates θ, φ defined from the x -axis. The range for both variables, θ and φ , are divided into N_θ and N_φ points. The range for t is divided into N_t points. The propagator is then represented by $q_{i,j,k}^n = q(\bar{x}_i, \theta_j, \varphi_k, t_n)$

On the basis of the current knowledge $q_{i,j,k}^n$, we calculate the next step by evaluating

$$q_{i,j,k}^{n+1} = q_{i,j,k}^n + \hat{H}_1 q_{i,j,k}^n + \hat{H}_2 q_{i,j,k}^n + \hat{H}_3 q_{i,j,k}^n \quad (49)$$

where the operator $\hat{H}_1 = \frac{L}{2\lambda} \Delta t \nabla_{\mathbf{u}}^2$ and $\hat{H}_3 = -\Delta t W_{i,j,k}$. Using the beam-warming upward method, for the $u_x > 0$ region we have

$$\begin{aligned}\hat{H}_2 q_{i,j,k}^n &= -\frac{\Delta t}{\Delta x} u_x (3q_{i,j,k}^n - 4q_{i-1,j,k}^n + q_{i-2,j,k}^n) \\ &\quad + \frac{1}{2} u_x \left(\frac{\Delta t}{\Delta x} \right)^2 (q_{i,j,k}^n - 2q_{i-1,j,k}^n + q_{i-2,j,k}^n),\end{aligned}\quad (50)$$

and for the $u_x < 0$ region we have

$$\begin{aligned}\hat{H}_2 q_{i,j,k}^n &= -\frac{\Delta t}{\Delta x} u_x (3q_{i,j,k}^n - 4q_{i+1,j,k}^n + q_{i+2,j,k}^n) \\ &\quad + \frac{1}{2} u_x \left(\frac{\Delta t}{\Delta x} \right)^2 (q_{i,j,k}^n - 2q_{i+1,j,k}^n + q_{i+2,j,k}^n).\end{aligned}\quad (51)$$

Grid points across the slit – The density profile is sharp near the wall boundaries of the slit. To achieve a better precision, we divide the space for \bar{x} , $[0, 1]$, nonuniformly. A variable transformation is made

$$\xi(\bar{x}) = \tan \left[(\pi - \gamma) \left(\bar{x} - \frac{1}{2} \right) \frac{L}{H} \right]. \quad (52)$$

Inversely we have

$$\bar{x}(\xi) = \left[\frac{1}{2} + \frac{\arctan(\xi)}{\pi - \gamma} \right]. \quad (53)$$

The parameter ξ is divided evenly in the range $[-\tan[(\pi - \gamma)/2], \tan[(\pi - \gamma)/2]]$ by N_x representative points. The spatial derivative term in (41) is replaced by

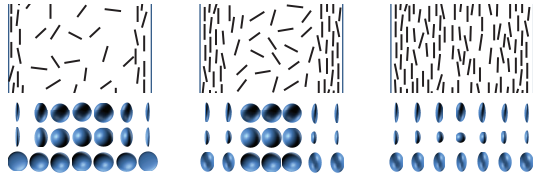
$$\frac{d}{d\bar{x}} = \frac{d\xi}{d\bar{x}} \frac{d}{d\xi} = \frac{(\pi - \gamma)L}{H} (1 + \xi^2) \frac{d}{d\xi}. \quad (54)$$

One can show that in the \bar{x} space, more representative points are placed near the wall boundaries. The parameter γ controls the grid distribution and adopts different values in the calculation.

In most calculation, we used $(N_x, N_\varphi, N_\theta, N_t, \gamma) = (51, 72, 37, 501, 0.5)$. For systems with large α we used $(51, 36, 19, 2001, 0.5)$.

TOC FIGURE: Surface-Induced Phase Transitions of Wormlike Chains in Slit Confinement

Shiwei Ye, Pingwen Zhang, and Jeff Z. Y. Chen



As the overall density increases, a semiflexible polymer fluid confined in slit displays three orientational states, stage by stage. The main-axis orientational distributions of different states near the surface have different characteristics.